ACS Energy LETTERS

http://pubs.acs.org/journal/aelccp

LETTER

Band Tailing and Deep Defect States in $CH_3NH_3Pb(I_{1-x}Br_x)_3$ Perovskites As Revealed by Sub-Bandgap Photocurrent

Carolin M. Sutter-Fella,[†,‡,∥,⊥] D. Westley Miller,[#,⊥] Quynh P. Ngo,[†,‡] Ellis T. Roe,[#] Francesca M. Toma,[∥] Ian D. Sharp,[∥] Mark C. Lonergan,[*,§] and Ali Javey[*,†,‡]

[†]Electrical Engineering and Computer Sciences, University of California, Berkeley, California 94720, United States
[‡]Materials Sciences Division, Lawrence Berkeley National Laboratory, Berkeley, California 94720, United States
[∥]Chemical Sciences Division, Lawrence Berkeley National Laboratory, Berkeley, California 94720, United States
[#]Department of Physics, University of Oregon, Eugene, Oregon 97403, United States
[§]Department of Chemistry and Biochemistry, University of Oregon, Eugene, Oregon 97403, United States

Supporting Information

ABSTRACT: Organometal halide perovskite semiconductors have emerged as promising candidates for optoelectronic applications because of the outstanding charge carrier transport properties, achieved with low-temperature synthesis. Here, we present highly sensitive sub-bandgap external quantum efficiency (EQE) measurements of Au/spiro-OMeTAD/$CH_3NH_3Pb(I_{1-x}Br_x)_3$/$TiO_2$/FTO/glass photovoltaic devices. The room-temperature spectra show exponential band tails with a sharp onset characterized by low Urbach energies (E_u) over the full halide composition space. The Urbach energies are 15−23 meV, lower than those for most semiconductors with similar bandgaps (especially with E_g > 1.9 eV). Intentional aging of $CH_3NH_3Pb(I_{1-x}Br_x)_3$ for up to 2300 h, reveals no change in E_u, despite the appearance of the PbI_2 phase due to decomposition, and confirms a high degree of crystal ordering. Moreover, sub-bandgap EQE measurements reveal an extended band of sub-bandgap electronic states that can be fit with one or two point defects for pure $CH_3NH_3PbI_3$ or mixed $CH_3NH_3Pb(I_{1-x}Br_x)_3$ compositions, respectively. The study provides experimental evidence of defect states close to the midgap that could impact photocarrier recombination and energy conversion efficiency in higher bandgap $CH_3NH_3Pb(I_{1-x}Br_x)_3$ alloys.

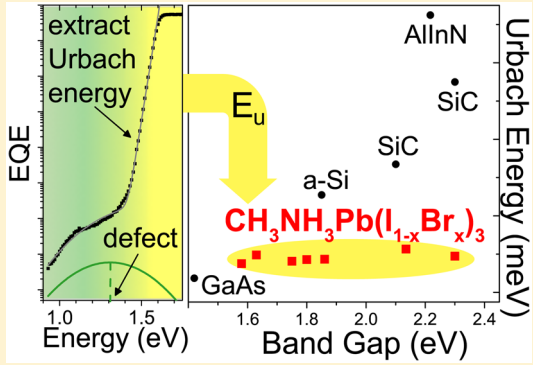

Organometal halide perovskites, with the general formula ABX_3, have generated enormous interest over the last 7 years as their solar cell power conversion efficiencies have increased from 3.8% in 2009[1] to the current world record of 22.1%.[2] Much of this progress has been realized by composition engineering at the A site with cations[3] including $CH(NH_2)_2^+$, $CH_3NH_3^+$, and Cs^+, at the B site with Pb^{2+} and Sn^{2+} cations,[4] and at the X site with I^-, Br^-, and Cl^- anions.[5,6] These changes have allowed researchers to increase photovoltaic power conversion efficiencies and chemical stabilities, as well as engineer the bandgap (E_g) for use in high-efficiency tandem photovoltaic devices.

Despite the intense interest in composition engineering, the effects of alloying on structural disorder and the densities of states (DOS), particularly within the bandgap, are not well documented. Their characterization is of central importance to identifying factors that contribute to efficiency loss and instability for a number of reasons. First, defects cause nonradiative recombination and modify the band alignment.[7] Second, there is a growing consensus that current−voltage hysteresis and photocurrent transients in organometal perovskite solar cells are due to defect states and related mobile ionic species.[7,8] Third, alloying might be expected to increase disorder in a crystal as the variety of possible defect states is increased. Importantly, the optical band edge, characterized by the Urbach energy (E_u),[9] can be broadened by disorder in the crystal lattice (or by impurities). Low Urbach energies are highly desirable for any semiconductor used in optoelectronic devices. Finally, the evolution of defect states and structural disorder upon aging could play a role in cell degradation.

Received: December 23, 2016
Accepted: February 15, 2017
Published: February 15, 2017

DOI: 10.1021/acsenergylett.6b00727
ACS Energy Lett. 2017, 2, 709−715

Probing the role of defects and disorder on optoelectronic properties requires sensitive spectroscopic probes. Defect transitions typically have much longer absorption lengths than interband transitions, therefore requiring analysis of optical absorption over several orders of magnitude below that at E_g. To this end, photothermal deflection spectroscopy (PDS)[10,11] and Fourier transform photocurrent spectroscopy (FTPS)[10] have been performed on isolated thin films, and sub-bandgap external quantum efficiency (EQE), transient photocapacitance, and transient photocurrent measurements have been applied to full photovoltaic devices.[12,13]

For $CH_3NH_3PbI_3$ films, previous PDS and FTPS measurements have shown purely exponential absorptance behavior with steep slopes that correspond to low values of E_u (~15 meV) and without the signatures of deep states within the bandgap for up to 4 orders of magnitude of response below E_g.[10] Similarly low values of E_u have been observed for $CH_3NH_3PbBr_3$ films by PDS (~25 meV)[11] and devices by photocurrent spectroscopy (~14 meV).[14] Values on mixed bromide/iodide alloys $CH_3NH_3Pb(I_{1-x}Br_x)_3$ have been more varied. Sadhanala et al. observed higher values of E_u at intermediate x with a peak of 90 meV for $x = 0.8$.[11] In contrast, Hoke et al. observed low values of $E_u = 12-17$ meV over nearly the full range of x, with an outlier at $x = 0.5$.[14]

Although the methods described above have been successful at characterizing E_u in $CH_3NH_3Pb(I_{1-x}Br_x)$ materials and solar cells, the signatures of electronically active defect states residing deep in the gap are rarely observed. In this regard, highly sensitive sub-bandgap EQE is a particularly powerful approach because it is capable of probing ultralow photocurrents due to sub-bandgap absorption that can be several orders of magnitude weaker than absorption at E_g. High sensitivity is enabled by using a high-throughput monochromator, a low-noise-current preamplifier, and careful filtering of above-bandgap stray light, allowing investigation of the sub-bandgap DOS (see the Supporting Information for experimental details). Indeed, this method has recently been applied to $CH_3NH_3PbI_3$ solar cells to reveal a defect band at 1.34 eV with varying density that was linked to photovoltaic characteristics.[12]

Here, we present sub-bandgap EQE measurements of Au/spiro-OMeTAD/$CH_3NH_3Pb(I_{1-x}Br_x)_3$/$TiO_2$/FTO/glass photovoltaic devices at room temperature and extending over the full halide composition space ($0 \leq x \leq 1$). In addition, we assess the impact of long-term aging of devices under atmospheric conditions, as monitored via formation of PbI_2, on photoluminescence quantum yields (PLQYs) and Urbach energies. Samples were aged for up to 2300 h in a typical laboratory environment with a temperature of 22 ± 1 °C and a relative humidity of 50 ± 7%. For all compositions, we found Urbach energies in the range of 15−23 meV that remain approximately constant throughout the experiment. Moreover, we found direct evidence of sub-bandgap electronic states within the perovskite light absorbers. For pure $CH_3NH_3PbI_3$, a single, relatively shallow state was observed. With increasing Br content, this state moves closer to the midgap while another shallow defect is revealed. If the densities of defect states near midgap cannot be controlled, then they will likely enhance Shockley−Read−Hall recombination in higher bandgap perovskites and potentially limit device performance. Our results provide important insight into the defect characteristics of the explored perovskite compositions, with implications for understanding disorder- and defect-induced performance limits.

$CH_3NH_3Pb(I_{1-x}Br_x)_3$ films on FTO/TiO_2 substrates were synthesized by a two-step, low-pressure, vapor-assisted, solution process (LP-VASP)[15,16] that yields high material uniformity and quality, with previously reported solar cell power conversion efficiencies of up to 19%.[17] In brief, the process starts with spin-coating and drying of the PbI_2/$PbBr_2$ precursor on the substrate in a N_2 atmosphere for 15 min at 110 °C and is followed by annealing in CH_3NH_3I and CH_3NH_3Br vapor for 2 h at 120 °C (schematic inset of Figure 1a; details on device processing can be found in the Supporting Information and ref 17). This process allows access to the full halide composition space and results in the expected decrease of the lattice parameter with increasing Br content, as evaluated by the (110) X-ray diffraction (XRD) peak angle. In Figure 1a, the (110) peak angle is plotted versus the halide composition of the film, as measured by energy-dispersive X-ray spectroscopy (10 kV, FEI Quanta FEG 250), and is approximately linear over this small range of angles. The halide composition, x, in $CH_3NH_3Pb(I_{1-x}Br_x)_3$ was related to the optical bandgap as described by the empirical equation $E_g(x) = 1.598 + 0.36x + 0.34x^2$ and is displayed as the upper x-axis in Figure 1a.[15] As mentioned above, sub-bandgap EQE measurements were

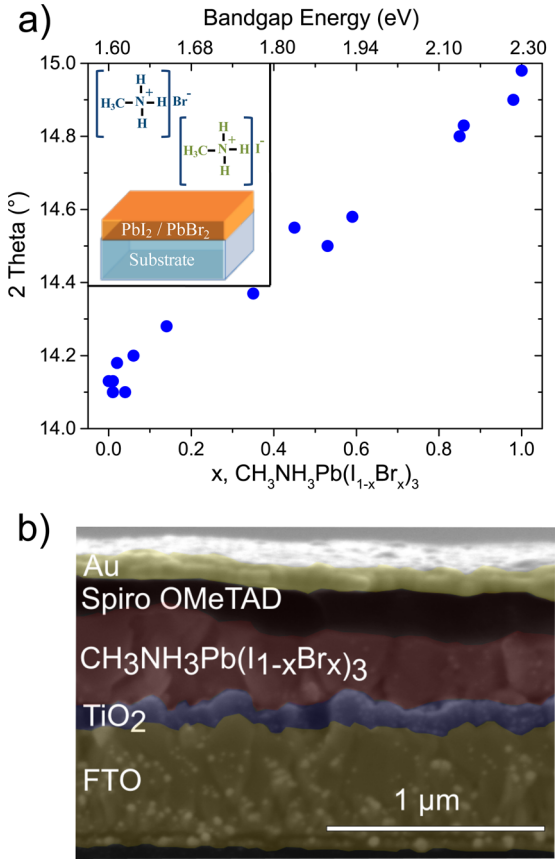

Figure 1. (a) Change in the lattice parameter, as evaluated by the (110) XRD peak angle, plotted versus the halide composition, x, determined by EDX measurements. The methylammonium lead halide ($CH_3NH_3Pb(I_{1-x}Br_x)_3$) perovskite films were prepared by the vapor-assisted solution process (schematic inset). The upper x-axis provides the bandgap corresponding to composition, calculated according to ref 15. (b) False colored cross-sectional scanning electron microscopy image of a typical planar Au/spiro-OMeTAD/$CH_3NH_3Pb(I_{1-x}Br_x)_3$/$TiO_2$/FTO photovoltaic device fabricated for this study.

DOI: 10.1021/acsenergylett.6b00727
ACS Energy Lett. 2017, 2, 709−715

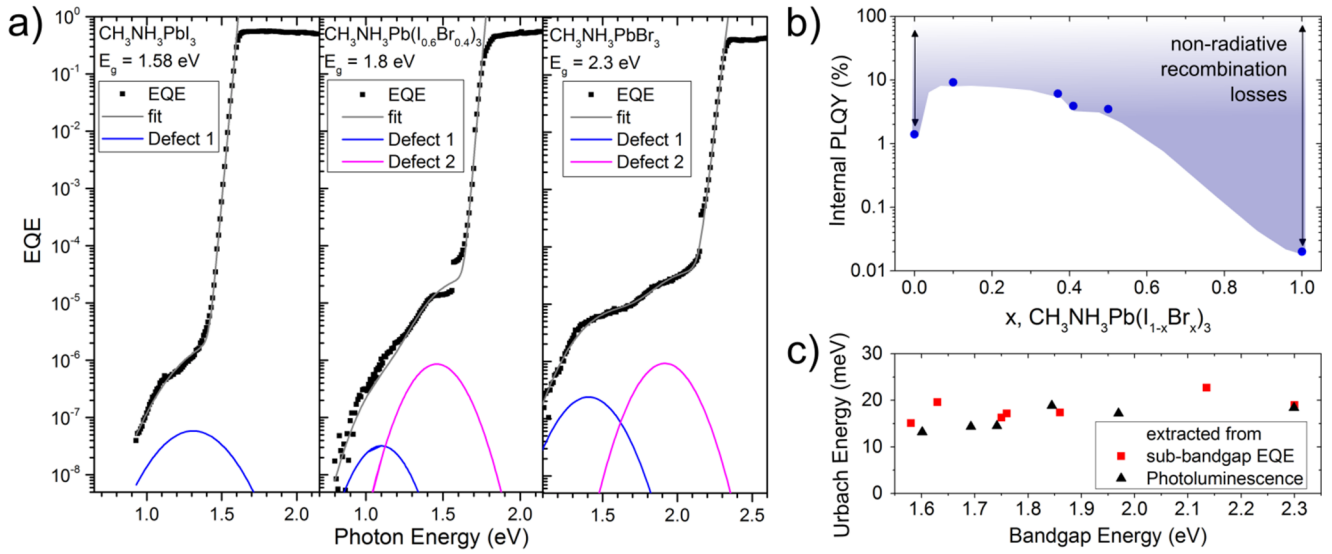

Figure 2. (a) Sub-bandgap EQE spectra for x = 0, 0.4, and 1 reveal the presence of electronically active defects. Fits to the data are shown as solid gray lines, with the underlying Gaussian defect distributions shown as solid blue and magenta lines. (b) Internal PLQY extracted at 1 sun illumination for different $CH_3NH_3Pb(I_{1-x}Br_x)_3$ compositions. The shaded area illustrates nonradiative recombination losses. (c) Summary of Urbach energies extracted from EQE and PL measurements plotted against the bandgap. The investigated $CH_3NH_3Pb(I_{1-x}Br_x)_3$ films show consistently low Urbach energies (E_u) between 15 and 23 meV over the full bandgap range of $1.6 \leq E_g \leq 2.3$ eV.

performed on photovoltaic devices. We fabricated the full stack of Au/spiro-OMeTAD/$CH_3NH_3Pb(I_{1-x}Br_x)_3$/$TiO_2$/FTO/glass with a planar device architecture, as illustrated in the cross-sectional scanning electron microscopy image in Figure 1b.

The sub-bandgap EQE was measured using long-pass filters to limit above-bandgap stray light from a scanning monochromator to 1 part in 10^7 throughout most of the spectral range (more experimental details can be found in the Supporting Information and in ref 12). Given that light-induced halide segregation has been reported to create I- and Br-rich domains,[14,18] it is important to note that the monochromatic light intensity used during EQE measurements was <0.04 mW/cm^2 above the bandgap of all samples examined. The light intensity varied over the spectral measurement and was below 0.4 mW/cm^2 at 0.8 eV, 0.04 mW/cm^2 at 1.6 eV, and 0.01 mW/cm^2 at 2.3 eV. This is much lower than the 10−100 mW/cm^2 used in the studies in which varying degrees of light-induced halide segregation were observed.[14,15,18] The proposed mechanisms for halide segregation are predicated on the generation of mobile charges and ions; thus, low irradiances may limit halide segregation during the measurement. Furthermore, according to prior work, halide segregation in these alloys is fully reversible within a few minutes of relaxation in the dark.[14] Because the EQE measurements reported here are performed at least 5 min after exposure to above-bandgap light more intense than that used for the measurement itself and the sub-bandgap portion requires hours of data collection, the role of halide segregation should be limited. Nonetheless, light-induced halide segregation in mixed I/Br samples cannot be fully excluded and may contribute, in parallel to defect responses, to sub-bandgap absorption. However, transitions in the samples with x = 0 and 1 and below 1.59 eV cannot be explained by the formation of I-rich domains.

Representative sub-bandgap EQE spectra of $CH_3NH_3Pb(I_{1-x}Br_x)_3$ devices (with x = 0, 0.4, and 1) are shown in Figure 2a together with the underlying Gaussian defect distributions plotted as solid blue and magenta lines (more sub-bandgap EQE spectra are illustrated in Figure S1 as well as full EQE spectra on a linear scale in Figure S2, Supporting Information). They reveal photocurrent due to optical transitions in the bandgap that likely involve point defects within the perovskite thin films. Sub-bandgap defect-related transitions in the EQE spectra (EQE_d) were fit using a function of the form

$$EQE_d \propto 1 + \mathrm{erf}\left(\frac{E - E_d}{\sigma_d\sqrt{2}}\right)$$

where E_d is the optical transition energy of the defect, E is the incident photon energy, and σ_d is the standard deviation of the underlying Gaussian energy density of states associated with a point defect. This functional form is consistent with absorption due to a transition from a Gaussian defect to the valence or conduction band and has been used to describe sub-bandgap absorption spectra of many semiconductors (more information is given in the Supporting Information).[19,20] For pure $CH_3NH_3PbI_3$, the best fit was obtained using a single defect model. However, with increasing Br content, the bandgap opens and a second defect-related transition emerges, requiring the use of a two-defect model to describe the response. All defect positions given in the following are the optical transition energies with respect to a band edge, though the technique does not provide information about the carrier type. The defect position (E_d) for the sample with x = 0 was observed at 1.36 ± 0.06 eV. For the sample with x = 0.4, the two defects were centered at 1.07 ± 0.06 and 1.43 ± 0.05 eV, and for the sample with x = 1, they were located at 1.42 ± 0.03 and 1.89 ± 0.04 eV, respectively. Because the exceedingly low photocurrents measured in sub-bandgap EQE could be generated in any part of the device, reference measurements were performed on spiro-OMeTAD and TiO_2 photoconductors (glass/FTO/spiro-OMeTAD/Au and glass/FTO/TiO_2/Ti, respectively) under identical conditions. The spiro-OMeTAD photoconductor showed a weak sub-bandgap response centered at 2.2 eV (see Supporting Information Figure S3), which is higher in energy

DOI: 10.1021/acsenergylett.6b00727
ACS Energy Lett. 2017, 2, 709−715

than any defect response observed from perovskite-containing photovoltaic devices. No sub-bandgap response was observed from TiO_2. While the TiO_2 photoconductor would be expected to show a band-edge optical response in the ultraviolet, the light source provided insufficient intensity in this spectral range and did not produce any measurable photocurrent. On the basis of these reference measurements, it is concluded that the sub-bandgap response detected from full photovoltaic device stacks is generated within the $CH_3NH_3Pb(I_{1-x}Br_x)_3$ absorber layers. While the sub-bandgap EQE response corresponds to transitions from bound to free electronic states that generate a photocurrent, it does not indicate whether the observed transitions are associated with trapped holes that are excited to the valence band or trapped electrons that are excited to the conduction band. Therefore, further research will be required to identify the specific nature of these defects, as well as their energetic positions on an absolute scale relative to each band edge, as a function of composition. Regardless of the exact defect positions, the observed sub-bandgap responses suggest that the higher bandgap alloys tend to form defects closer to the midgap. For example, the 1.36 eV defect observed in the $x = 0$ sample corresponds to a state that is 220 meV from a band edge and 570 meV away from the midgap position. In stark contrast, the 1.42 eV transition seen in the $x = 1$ sample is positioned 880 meV away from a band edge and only 270 meV from the middle of the bandgap. Defects closer to the midgap are much more efficient recombination centers, even for the same defect density.

In contrast to our finding, some previous density functional theory (DFT) studies have found that deep defects should have prohibitively high formation energies in organolead iodide perovskites.[21,22] However, others predict a high density of deep traps under I-rich synthesis conditions due to the formation of I-on-Pb antisite (I_{Pb}) defects with a formation energy < 0.2 eV.[23] The 1.36, 1.43, and 1.42 eV transitions observed in the $x = 0$, 0.4, and 1 cells, respectively, are within one standard deviation of each other and are a reasonably close match for the V_{Pb} (−1/−2) transition energy predicted as the dominant defect for $x = 0$.[21] Furthermore, this matches a previously observed defect in $x = 0$ perovskites grown by another technique and whose density was correlated with steady-state performance losses and large $J-V$ hysteresis.[12] Our findings are most consistent with the V_{Pb} appearing at near the same energy relative to the conduction band across the samples studied. The 1.89 eV transition observed in the $x = 1$ cell is a close match for the V_{Pb} (0/−1) transition, which is predicted to be obscured by the valence band in $CH_3NH_3PbI_3$.[21] Previous studies have indicated that alloying $CH_3NH_3PbI_3$ with Br mostly shifts the energetic position of the valence band,[24,25] suggesting that such defect states would become optoelectronically active as the bandgap opens. Note that the jump in the data appearing near 1.55 eV (Figure 2a) is an artifact of the measurement due to the addition of a long-pass filter at that energy eliminating the contribution of above-bandgap stray light. The impact of stray light on our EQE spectra is discussed in great detail in the Supporting Information.

Both time-resolved photoluminescence (PL)[26] and PLQY[15] measurements corroborate the sub-bandgap EQE detection of deep defects by showing that trap-assisted recombination is the limiting mechanism at low illumination intensities, which are of relevance to the current work. In particular, the former study explained the monoexponential decay observed at low laser fluence by monomolecular (trap-assisted) recombination, and the latter study suggested that trap-assisted recombination limits the PLQY at illumination intensities of ≤1 sun for $0 \leq x \leq 1$. Figure 2b summarizes the internal PLQY extracted at 1 sun illumination for different $CH_3NH_3Pb(I_{1-x}Br_x)_3$ compositions measured on LP-VASP perovskite thin films. Further details on PLQY measurements are reported in the Supporting Information and have been published previously in ref 15. A PLQY of 100% would correspond to radiative recombination as the only recombination mechanism in the studied sample. PLQYs below 100% are indicative of nonradiative recombination losses. Figure 2b indicates significantly lower quantum yield in $CH_3NH_3PbBr_3$. As we have shown previously in our detailed PLQY analysis of $CH_3NH_3Pb(I_{1-x}Br_x)_3$ films, $CH_3NH_3PbBr_3$ seems to be limited by trap-assisted recombination over the full range of pump powers used (ref 15). However, from PLQY, it is not clear if the defect density is higher or if the depopulation of traps is significantly faster for $x = 1$. The combination of PLQY measurements (which probe inherent film properties), indicating trap-assisted recombination at low illumination intensities in the perovskite films (compare Supporting Information, Figure S4, and ref 15), and sub-bandgap EQE data, revealing the presence of deep defect states in the absorber layer (with increasing x) of active devices, suggests that deep defects could play an active role in affecting performance characteristics of optoelectronic devices incorporating $CH_3NH_3Pb(I_{1-x}Br_x)_3$.

The Urbach energies extracted from EQE measurements versus bandgap are provided in Figure 2c. Bandgaps were determined from Tauc plots[27] (further experimental details are described in the Supporting Information), resulting in values in the expected range of 1.58−2.3 eV. Here, we also report the Urbach energies of LP-VASP samples grown on glass substrates extracted from PL spectra using the van Roosbroeck−Shockley equation, where the optical emission rate is related to the absorption coefficient.[28] All EQE spectra display sharp absorption edges below E_g that translate into low Urbach energies (15−23 meV) and are in excellent agreement with those obtained from PL spectra (13−19 meV).

It is interesting to compare Urbach energies of $CH_3NH_3Pb(I_{1-x}Br_x)_3$ films to a range of technologically important inorganic semiconductors used in photovoltaic and other optoelectronic applications. The Urbach energies obtained in this study from fitting of sub-bandgap EQE data are plotted against their optical bandgaps, together with available literature values, in Figure 3. The bandgap range accessible with $CH_3NH_3Pb(I_{1-x}Br_x)_3$ is highlighted ($1.6 \leq E_g \leq 2.3$ eV) and clearly shows near-constant Urbach energies that are significantly lower than those in conventional semiconductors, especially for $E_g > 1.9$ eV. This is remarkable given the polycrystalline nature of the hybrid organic−inorganic perovskite thin films and the nature of the synthesis process, which does not exceed 120 °C and is performed on nonlattice matched substrates. Furthermore, the available literature data for Urbach energies in $CH_3NH_3Pb(I_{1-x}Br_x)_3$ yielded significantly higher Urbach energy values than those reported here for some of the mixed I/Br compositions (compare blue triangles in Figure 3).[11,14] Possibly, the synthesis method could play a role in defining disorder, particularly in compositionally complex mixed halide perovskites.

While it is well established that methylammonium lead halide perovskites decompose upon exposure to ambient air,[37] less is known about how this process impacts defects and disorder in the material. As mentioned earlier, the unencapsulated devices

DOI: 10.1021/acsenergylett.6b00727
ACS Energy Lett. 2017, 2, 709−715

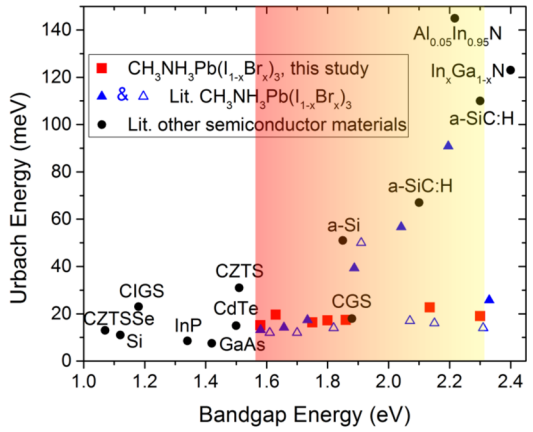

Figure 3. Urbach energies versus bandgap with the range accessible by $CH_3NH_3Pb(I_{1-x}Br_x)_3$ perovskites highlighted in the shaded region. Urbach energies from $CH_3NH_3Pb(I_{1-x}Br_x)_3$ perovskites in this study are shown as red squares, and those from literature data are shown as blue triangles.[11,14] Also shown are a range of technologically important semiconductors (black dots): CZTSSe (Se-rich $Cu_2ZnSn(S,Se)_4$),[20] Si,[10] CIGS ($Cu(In,Ga)Se_2$),[19] InP,[29] GaAs,[30] CdTe,[31] CZTS (S-rich Cu_2ZnSnS_4),[20] CGS ($CuGaSe_2$),[32] a-Si,[33] a-SiC:H,[34] $Al_{0.05}In_{0.95}N$,[35] and $In_xGa_{1-x}N$ (In-rich, graded In profile).[36]

in this study were aged in the dark under laboratory conditions for up to 2300 h. Reaction with atmospheric species leaves PbI_2 as a primary solid-state product. Therefore, XRD can be used to probe changes of the film in fully assembled devices, with the evolution of the (001) PbI_2/(110) perovskite ($PbBr_2$/perovskite for $x = 1$) XRD integrated peak area ratio providing a useful metric for tracking decomposition as a function of time after synthesis. As shown in Figure 4a (and Figure S5a, Supporting Information), XRD reveals a general trend of increasing PbI_2 with time for mixed I/Br compositions, while the pure I- and Br-perovskites exhibit very little decomposition during the investigated time interval. In parallel, we recorded the sub-bandgap EQE data on the aged samples and extracted the Urbach energies. Figure 4b displays the evolution of the Urbach energies over time for different $CH_3NH_3Pb(I_{1-x}Br_x)_3$ devices. The data points are connected for better visibility and show approximately constant Urbach energies, in the range of 15−23 meV, for over 2300 h of degradation. This result indicates that aging and decomposition do not significantly increase disorder and band tail states within the material.

Examination of the EQE response further below the bandgap reveals that aging does not increase concentrations of energetically deeper defect states, as shown in Figure 4c. For the case of $CH_3NH_3PbI_3$-based devices, the defect-related response appears to be unaffected by aging for up to 791 h, whereas for $CH_3NH_3Pb(I_{0.1}Br_{0.9})_3$-based devices the density of defect states seems to decrease after 706 and 2316 h of aging, during which time this mixed halide sample partially decomposes, as indicated by the formation of PbI_2. This finding is consistent with an observed increase in internal PLQY after several weeks of aging, which implies lower defect-mediated recombination rates at low illumination intensities (Supporting Information Figure S4). This increase of PL efficiency with aging time can be explained by passivation of interface states by formation of PbI_2.[38,39] After longer degradation times, it must be considered that the actual active absorptive volume within the device is reduced due to consumption of the perovskite phase and formation of PbI_2, which leads to lower overall light absorption and, thus, lower photocurrent response. It is also important to note that PbI_2 precipitation was highly nonuniform over the sample (compare the photograph in Figure S5b, Supporting Information) and XRD patterns represent an average over regions much larger than the device area probed by EQE (i.e., XRD samples regions with and without the Au contact layers, whereas EQE measurements only sample the device active area under the Au contacts).

In summary, we have presented sub-bandgap EQE measurements on Au/spiro-OMeTAD/$CH_3NH_3Pb(I_{1-x}Br_x)_3$/$TiO_2$/FTO/glass photovoltaic devices. All $CH_3NH_3Pb(I_{1-x}Br_x)_3$ compositions, with corresponding bandgaps of $1.6 \leq E_g \leq 2.3$ eV, exhibit low Urbach energies in the range of 15−23 meV. These Urbach energies are significantly lower than those of most conventional inorganic semiconductors with similar bandgaps, especially for $E_g > 1.9$ eV, and are not affected by long-term aging of perovskite-based photovoltaic devices (as indicated by the co-presence of PbI_2). Moreover, this study

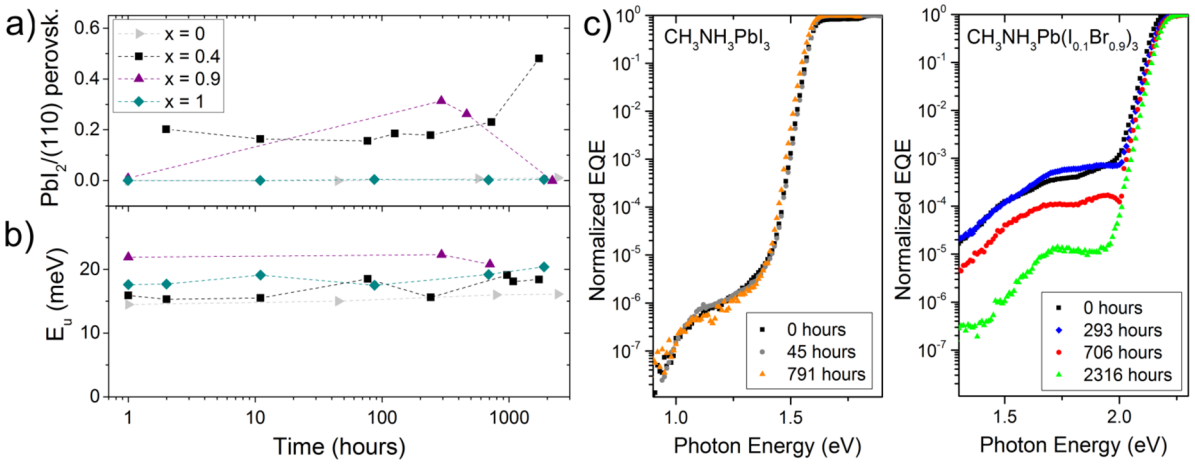

Figure 4. (a) Repeated XRD measurements showing the integrated XRD peak ratio of the (001) PbI_2/(110) perovskite ($PbBr_2$/perovskite for $x = 1$) phase as a function of time for different $CH_3NH_3Pb(I_{1-x}Br_x)_3$ compositions. (b) Time evolution of Urbach energies under aging, as extracted from sub-bandgap EQE measurements. (Data points in (a) and (b) are connected as a guide for the eye.) (c) Sub-bandgap EQE spectra taken on the same photovoltaic devices as-received (0 h) and after extended aging under laboratory conditions.

DOI: 10.1021/acsenergylett.6b00727
ACS Energy Lett. 2017, 2, 709−715

reveals the presence of sub-bandgap defect states for all compositions. These states can be fit with one or two point defects for pure $CH_3NH_3PbI_3$ or mixed $CH_3NH_3Pb(I_{1-x}Br_x)_3$ compositions, respectively. With increasing Br content, the second state emerges, and the observed defect responses indicate that the higher bandgap alloys are characterized by deep level defects with states close to the midgap. The combination of sub-bandgap EQE, which can directly detect midgap states, and PL-based studies, which can identify recombination pathways and probabilities, provides a future path toward assessing the roles of synthesis and processing on efficiency-limiting recombination centers in the material.

■ ASSOCIATED CONTENT

Supporting Information

The Supporting Information is available free of charge on the ACS Publications website at DOI: 10.1021/acsenergylett.6b00727.

Experimental section describing film formation, device processing, sensitive sub-bandgap EQE, including fitting of the spectra, and PLQY measurements; sub-bandgap EQE measurements on glass/FTO/spiro-OMeTAD/Au and glass/FTO/TiO_2/Ti photoconductors; full EQE spectra on a linear scale; photoluminescence quantum yield measurements on a $CH_3NH_3Pb(I_{0.9}Br_{0.1})_3$ film under pump-power-dependent illumination as-synthesized and remeasured after aging; and XRD measurements over time and a photograph of the aged sample (PDF)

■ AUTHOR INFORMATION

Corresponding Authors

*E-mail: lonergan@uoregon.edu (M.C.L.).
*E-mail: ajavey@berkeley.edu (A.J.).

ORCID

Carolin M. Sutter-Fella: 0000-0002-7769-0869
Ian D. Sharp: 0000-0001-5238-7487

Author Contributions

[⊥]The manuscript was written through contributions of all authors. All authors have given approval to the final version of the manuscript. C.M.S.-F. and D.W.M. contributed equally.

Notes

The authors declare no competing financial interest.

■ ACKNOWLEDGMENTS

Perovskite synthesis, characterization, and device fabrication were performed with support by the Solar Photochemistry Program of the U.S. Department of Energy, Office of Science, Office of Basic Energy Sciences, Division of Chemical, Geological and Biosciences under Contract No. DE-AC02-05CH11231 (I.D.S.) and by the Laboratory Directed Research and Development Program of Lawrence Berkeley National Laboratory under U.S. Department of Energy Contract Number DE-AC02-05CH11231 (F.M.T). The optical characterization and quantum yield measurements were supported by the Electronic Materials program, funded by the Director, Office of Science, Office of Basic Energy Sciences, Materials Sciences and Engineering Division of the U.S. Department of Energy under Contract No. DE-AC02-05CH11231. Some electrical performance measurements were performed at the Molecular Foundry, which is supported by the Office of Science, Office of Basic Energy Sciences, of the U.S. Department of Energy under Contract No. DE-AC02-05CH11231. The sub-bandgap EQE measurements and analyses presented were funded by the Office of Basic Energy Sciences of the U.S. Department of Energy through DE-SC0012363. This work utilized equipment in the SuNRISE Photovoltaic Laboratory supported by Oregon BEST. C.M.S.-F. acknowledges financial support from the Swiss National Science Foundation (P2EZP2_155586).

■ REFERENCES

(1) Kojima, A.; Teshima, K.; Shirai, Y.; Miyasaka, T. Organometal Halide Perovskites as Visible-Light Sensitizers for Photovoltaic Cells. *J. Am. Chem. Soc.* **2009**, *131*, 6050−6051.

(2) Zhang, W.; Eperon, G. E.; Snaith, H. J. Metal Halide Perovskites for Energy Applications. *Nat. Energy* **2016**, *1*, 16048.

(3) Saliba, M.; Matsui, T.; Seo, J.-Y.; Domanski, K.; Correa-Baena, J.-P.; Nazeeruddin, M. K.; Zakeeruddin, S. M.; Tress, W.; Abate, A.; Hagfeldt, A.; Grätzel, M. Cesium-Containing Triple Cation Perovskite Solar Cells: Improved Stability, Reproducibility and High Efficiency. *Energy Environ. Sci.* **2016**, *9*, 1989−1997.

(4) Eperon, G. E.; Leijtens, T.; Bush, K. A.; Green, T.; Wang, J. T.-W.; McMeekin, D. P.; Volonakis, G.; Milot, R. L.; Slotcavage, D. J.; Belisle, R.; et al. Perovskite-Perovskite Tandem Photovoltaics with Ideal Bandgaps. *Science* **2016**, *354*, 861.

(5) Noh, J. H.; Im, S. H.; Heo, J. H.; Mandal, T. N.; Seok, S. I. Chemical Management for Colorful, Efficient, and Stable Inorganic−Organic Hybrid Nanostructured Solar Cells. *Nano Lett.* **2013**, *13*, 1764−1769.

(6) Sadhanala, A.; Ahmad, S.; Zhao, B.; Giesbrecht, N.; Pearce, P. M.; Deschler, F.; Hoye, R. L. Z.; Gödel, K. C.; Bein, T.; Docampo, P.; et al. Blue-Green Color Tunable Solution Processable Organolead Chloride−Bromide Mixed Halide Perovskites for Optoelectronic Applications. *Nano Lett.* **2015**, *15*, 6095−6101.

(7) Ball, J. M.; Petrozza, A. Defects in Perovskite-Halides and Their Effects in Solar Cells. *Nat. Energy* **2016**, *1*, 16149.

(8) Unger, E. L.; Hoke, E. T.; Bailie, C. D.; Nguyen, W. H.; Bowring, A. R.; Heumüller, T.; Christoforo, M. G.; McGehee, M. D. Hysteresis and Transient Behavior in Current−voltage Measurements of Hybrid-Perovskite Absorber Solar Cells. *Energy Environ. Sci.* **2014**, *7*, 3690−3698.

(9) Urbach, F. The Long-Wavelength Edge of Photographic Sensitivity and of the Electronic Absorption of Solids. *Phys. Rev.* **1953**, *92*, 1324−1324.

(10) De Wolf, S.; Holovsky, J.; Moon, S.-J.; Löper, P.; Niesen, B.; Ledinsky, M.; Haug, F.-J.; Yum, J.-H.; Ballif, C. Organometallic Halide Perovskites: Sharp Optical Absorption Edge and Its Relation to Photovoltaic Performance. *J. Phys. Chem. Lett.* **2014**, *5*, 1035−1039.

(11) Sadhanala, A.; Deschler, F.; Thomas, T. H.; Dutton, S. E.; Goedel, K. C.; Hanusch, F. C.; Lai, M. L.; Steiner, U.; Bein, T.; Docampo, P.; et al. Preparation of Single-Phase Films of $CH_3NH_3Pb(I_{1-x}Br_x)_3$ with Sharp Optical Band Edges. *J. Phys. Chem. Lett.* **2014**, *5*, 2501−2505.

(12) Miller, D. W.; Eperon, G. E.; Roe, E. T.; Warren, C. W.; Snaith, H. J.; Lonergan, M. C. Defect States in Perovskite Solar Cells Associated with Hysteresis and Performance. *Appl. Phys. Lett.* **2016**, *109*, 153902.

(13) Wang, H.-P.; Sutter-Fella, C. M.; Lobaccaro, P.; Hettick, M.; Zheng, M.; Lien, D.-H.; Miller, D. W.; Warren, C. W.; Roe, E. T.; Lonergan, M. C.; et al. Increased Optoelectronic Quality and Uniformity of Hydrogenated P-InP Thin Films. *Chem. Mater.* **2016**, *28*, 4602−4607.

(14) Hoke, E. T.; Slotcavage, D. J.; Dohner, E. R.; Bowring, A. R.; Karunadasa, H. I.; McGehee, M. D. Reversible Photo-Induced Trap Formation in Mixed-Halide Hybrid Perovskites for Photovoltaics. *Chem. Sci.* **2015**, *6*, 613−617.

(15) Sutter-Fella, C. M.; Li, Y.; Amani, M.; Ager, J. W.; Toma, F. M.; Yablonovitch, E.; Sharp, I. D.; Javey, A. High Photoluminescence

DOI: 10.1021/acsenergylett.6b00727
ACS Energy Lett. 2017, 2, 709−715

Quantum Yield in Band Gap Tunable Bromide Containing Mixed Halide Perovskites. *Nano Lett.* **2016**, *16*, 800−806.
(16) Li, Y.; Cooper, J. K.; Buonsanti, R.; Giannini, C.; Liu, Y.; Toma, F. M.; Sharp, I. D. Fabrication of Planar Heterojunction Perovskite Solar Cells by Controlled Low-Pressure Vapor Annealing. *J. Phys. Chem. Lett.* **2015**, *6*, 493−499.
(17) Li, Y.; Cooper, J. K.; Liu, W.; Sutter-Fella, C. M.; Amani, M.; Beeman, J. W.; Javey, A.; Ager, J. W.; Liu, Y.; Toma, F. M.; et al. Defective TiO_2 with High Photoconductive Gain for Efficient and Stable Planar Heterojunction Perovskite Solar Cells. *Nat. Commun.* **2016**, *7*, 12446.
(18) Bischak, C. G.; Hetherington, C. L.; Wu, H.; Aloni, S.; Ogletree, D. F.; Limmer, D. T.; Ginsberg, N. S. Origin of Reversible Photo-Induced Phase Separation in Hybrid Perovskites. *ArXiv160607366 Cond-Mat Physics* **2016**.
(19) Heath, J. T.; Cohen, J. D.; Shafarman, W. N.; Liao, D. X.; Rockett, A. A. Effect of Ga Content on Defect States in $CuIn_{1-x}Ga_xSe_2$ Photovoltaic Devices. *Appl. Phys. Lett.* **2002**, *80*, 4540−4542.
(20) Miller, D. W.; Warren, C. W.; Gunawan, O.; Gokmen, T.; Mitzi, D. B.; Cohen, J. D. Electronically Active Defects in the $Cu_2ZnSn(Se,S)_4$ Alloys as Revealed by Transient Photocapacitance Spectroscopy. *Appl. Phys. Lett.* **2012**, *101*, 142106.
(21) Yin, W.-J.; Shi, T.; Yan, Y. Unusual Defect Physics in $CH_3NH_3PbI_3$ Perovskite Solar Cell Absorber. *Appl. Phys. Lett.* **2014**, *104*, 063903.
(22) Yin, W.-J.; Shi, T.; Yan, Y. Unique Properties of Halide Perovskites as Possible Origins of the Superior Solar Cell Performance. *Adv. Mater.* **2014**, *26*, 4653−4658.
(23) Buin, A.; Pietsch, P.; Xu, J.; Voznyy, O.; Ip, A. H.; Comin, R.; Sargent, E. H. Materials Processing Routes to Trap-Free Halide Perovskites. *Nano Lett.* **2014**, *14*, 6281−6286.
(24) Schulz, P.; Edri, E.; Kirmayer, S.; Hodes, G.; Cahen, D.; Kahn, A. Interface Energetics in Organo-Metal Halide Perovskite-Based Photovoltaic Cells. *Energy Environ. Sci.* **2014**, *7*, 1377−1381.
(25) Butler, K. T.; Frost, J. M.; Walsh, A. Band Alignment of the Hybrid Halide Perovskites $CH_3NH_3PbCl_3$, $CH_3NH_3PbBr_3$ and $CH_3NH_3PbI_3$. *Mater. Horiz.* **2015**, *2*, 228−231.
(26) Stranks, S. D.; Burlakov, V. M.; Leijtens, T.; Ball, J. M.; Goriely, A.; Snaith, H. J. Recombination Kinetics in Organic-Inorganic Perovskites: Excitons, Free Charge, and Subgap States. *Phys. Rev. Appl.* **2014**, *2*, 34007.
(27) Tauc, J.; Grigorovici, R.; Vancu, A. Optical Properties and Electronic Structure of Amorphous Germanium. *Phys. Status Solidi B* **1966**, *15*, 627−637.
(28) van Roosbroeck, W.; Shockley, W. Photon-Radiative Recombination of Electrons and Holes in Germanium. *Phys. Rev.* **1954**, *94*, 1558−1560.
(29) Chen, K.; Kapadia, R.; Harker, A.; Desai, S.; Seuk Kang, J.; Chuang, S.; Tosun, M.; Sutter-Fella, C. M.; Tsang, M.; Zeng, Y.; et al. Direct Growth of Single-Crystalline III-V Semiconductors on Amorphous Substrates. *Nat. Commun.* **2016**, *7*, 10502.
(30) Johnson, S. R.; Tiedje, T. Temperature Dependence of the Urbach Edge in GaAs. *J. Appl. Phys.* **1995**, *78*, 5609−5613.
(31) Warren, C. W.; Li, J.; Wolden, C. A.; Meysing, D. M.; Barnes, T. M.; Miller, D. W.; Heath, J. T.; Lonergan, M. C. The Effect of Copper on the Sub-Bandgap Density of States of CdTe Solar Cells. *Appl. Phys. Lett.* **2015**, *106*, 203903.
(32) Cohen, J. D. *Identifying the Electronic Properties Relevant to Improving the Performance of High Band-Gap Copper Based I−III−VI2 Chalcopyrite Thin Film Photovoltaic Devices*; Subcontract Report NREL/SR-520-43909; 2008.
(33) van Veen, M. K.; Schropp, R. E. I. Beneficial Effect of a Low Deposition Temperature of Hot-Wire Deposited Intrinsic Amorphous Silicon for Solar Cells. *J. Appl. Phys.* **2003**, *93*, 121−125.
(34) Conde, J. P.; Chu, V.; da Silva, M. F.; Kling, A.; Dai, Z.; Soares, J. C.; Arekat, S.; Fedorov, A.; Berberan-Santos, M. N.; Giorgis, F.; Pirri, C. F. Optoelectronic and Structural Properties of Amorphous Silicon−Carbon Alloys Deposited by Low-Power Electron-Cyclotron Resonance Plasma-Enhanced Chemical-Vapor Deposition. *J. Appl. Phys.* **1999**, *85*, 3327−3338.
(35) Jiang, L. F.; Shen, W. Z.; Guo, Q. X. Temperature Dependence of the Optical Properties of AlInN. *J. Appl. Phys.* **2009**, *106*, 013515.
(36) Valdueza-Felip, S.; Bellet-Amalric, E.; Núñez-Cascajero, A.; Wang, Y.; Chauvat, M.-P.; Ruterana, P.; Pouget, S.; Lorenz, K.; Alves, E.; Monroy, E. High In-Content InGaN Layers Synthesized by Plasma-Assisted Molecular-Beam Epitaxy: Growth Conditions, Strain Relaxation, and In Incorporation Kinetics. *J. Appl. Phys.* **2014**, *116*, 233504.
(37) Tiep, N. H.; Ku, Z.; Fan, H. J. Recent Advances in Improving the Stability of Perovskite Solar Cells. *Adv. Energy Mater.* **2016**, *6*, 1501420.
(38) Chen, Q.; Zhou, H.; Song, T.-B.; Luo, S.; Hong, Z.; Duan, H.-S.; Dou, L.; Liu, Y.; Yang, Y. Controllable Self-Induced Passivation of Hybrid Lead Iodide Perovskites toward High Performance Solar Cells. *Nano Lett.* **2014**, *14*, 4158−4163.
(39) Jiang, F.; Rong, Y.; Liu, H.; Liu, T.; Mao, L.; Meng, W.; Qin, F.; Jiang, Y.; Luo, B.; Xiong, S.; et al. Synergistic Effect of PbI_2 Passivation and Chlorine Inclusion Yielding High Open-Circuit Voltage Exceeding 1.15 V in Both Mesoscopic and Inverted Planar $CH_3NH_3PbI_3(Cl)$-Based Perovskite Solar Cells. *Adv. Funct. Mater.* **2016**, *26*, 8119−8127.

DOI: 10.1021/acsenergylett.6b00727
ACS Energy Lett. 2017, 2, 709−715